SENSORS

Dynamic tactility by position-encoded spike spectrum

Taeyeong Kim[1], Jaehun Kim[2], Insang You[3], Joosung Oh[1], Sung-Phil Kim[2]*, Unyong Jeong[1]*

In fast and transient somatosensory processing, the relative timing of the selected spikes is more important than the spike frequency because the ensemble of the first spikes in the spike trains encodes the dynamic tactile information. Here, inspired by the functional effectiveness of the selected spikes, we propose an artificial dynamic sensory system based on position-encoded spike spectrum. We use a mixed ion-electron conductor to generate a potential spike signal. We design artificial receptors that have different ion relaxation times (τ); thus, a sequence of the spikes from the receptors creates a spike spectrum, providing the spatial information (position and motion trace) and the temporal information (speed and dynamic contact area). The artificial receptors can be incorporated by as much as 132/square centimeters by using only two global signal addressing lines for sensor operation. Structural simplicity of the device opens the possibility of scalable fabrication with dense receptor integration. With computational decoding of the position-encoded spike spectrum, the artificial sensory system can recognize complicated dynamic motions in real time. The high-resolution spatiotemporal tactile perception in the ionic artificial sensory system enables the real-time dynamic robotic manipulation.

INTRODUCTION

Electronic skin (E-skin) has been developed to realize the human cutaneous sensation (*1*). Applications are expected in various fields such as haptic devices (*2*, *3*), health monitoring (*4*, *5*), medical implants (*6*), sensory feedback for robotics (*7*, *8*), and prosthetics (*9*, *10*). The data acquisition of pixelated E-skin arrays is conventionally based on the sequential measurement of time division multiple access (TDMA) to the pixels at each measurement cycle (*11*, *12*). However, a highly integrated TDMA system suffers the readout delay (*13*, *14*) and large power consumption because of the continuous measurement (*15*) and necessarily requires high-level complexity in circuit design to integrate the switching units (*16*). Meanwhile, the event-driven spike generation in the human somatosensory system allows parallel data processing without the readout delay (*17*). At present, event-driven artificial sensory systems have generated spike trains by converting the resistance (or capacitance) changes from the sensor pixels through analog-to-digital converters (ADCs) (*18*–*20*). However, incorporating rigid or bulky converters is not desirable for flexible or deformable sensory systems, and it limits the spatial resolution of the pixels and makes the device structure complicated. Event-driven spike generation without the converters is thus desired to achieve structural simplicity and low power consumption in artificial sensory systems.

In the highly transient human somatosensory processes, spatiotemporal information is extracted from the spike trains of the multiple Meissner's afferents [fast-adapting type I (FA-I) afferents] (*21*). The first spikes that are temporally overlapping in the transmitted spike trains are selectively used for fast perception (stimulated position, force direction, object shape, etc.) of dynamic mechanical stimulation (*22*, *23*). Thus, for fast dynamic tactility, the relative timing of the selected spikes is more important than the spike frequency in the spike trains. Inspired by functional effectiveness of the selected spikes, we designed an artificial tactile system, called position-encoded spike spectrum (PESS) (Fig. 1A and Movie 1). When the artificial receptors are stimulated, potential spikes are generated and the spikes from different receptors are merged into a single channel to form the PESS. The PESS can be decoded in real time to identify each spike on the basis of the relaxation time (τ) of the spikes. The PESS consists of auxiliary spikes with a small τ (2 ms) and characteristic spikes with larger τ (≥10 ms), encoding the contact area and position of a contact object, respectively.

Here, we fabricated an artificial receptor consisting of a mixed ion-electron conductor (MIEC) and controlled ion dynamics to generate a unique potential spike (Fig. 1B). As the artificial receptor was stimulated, ion drift and ion polarization in the MIEC layer led to a potential spike. In the absence of stimulation, the ions were restored to their initial state through the drifts of electrons and ions. These spike generation and charge restoration were repeated by external stimulation. The ion drift, polarization, and electron drift can be described by the ion resistance (R_{ion}), the electrical double-layer capacitance (C_{dl}), and the electron resistance (R_{el}), respectively. The peak potential of the spike (V_{peak}) is inversely proportional to R_{ion}, and the τ of the spike is approximated by R_{ion} C_{dl} (Fig. 1C, fig. S1, and text S1). The event-driven spike generation of the artificial sensory system enabled real-time recognition (<5 ms) in response to dynamic stimuli such as slip and rolling of an object (Fig. 1D).

RESULTS

Spike profile modulation by controlling ion and electron dynamics

The resistance (R_{ion} and R_{el}) and the capacitance (C_{dl}) of the MIEC were adjusted to control V_{peak} and τ of the unit artificial receptor, respectively (Fig. 2A). The MIEC film was composed of an ionic liquid [1-butyl-3-methylimidazolium tetrafluoroborate (BMIM:BF_4)] and a conducting polymer [poly(3,4-ethylenedioxythiophene)-poly(styrene sulfonate) (PEDOT:PSS)], which were mixed in a photocrosslinked polymer matrix of poly(ethylene glycol) diacrylate (PEG-DA) (see Materials and Methods for the preparation details). R_{el} and R_{ion} were adjusted by the concentration of PEDOT:PSS and the ionic liquid. Then, PEDOT:PSS was spray-coated on the top and bottom sides of the MIEC film to form the volumetric capacitance

[1]Department of Materials Science and Engineering, Pohang University of Science and Technology (POSTECH), Pohang 37673, Republic of Korea. [2]Department of Biomedical Engineering, Ulsan National Institute of Science and Technology (UNIST), Ulsan 44919, Republic of Korea. [3]Department of Chemical Engineering, POSTECH, Pohang 37673, Republic of Korea.
*Corresponding author. Email: spkim@unist.ac.kr (S.-P.K); ujeong@postech.ac.kr (U.J.)

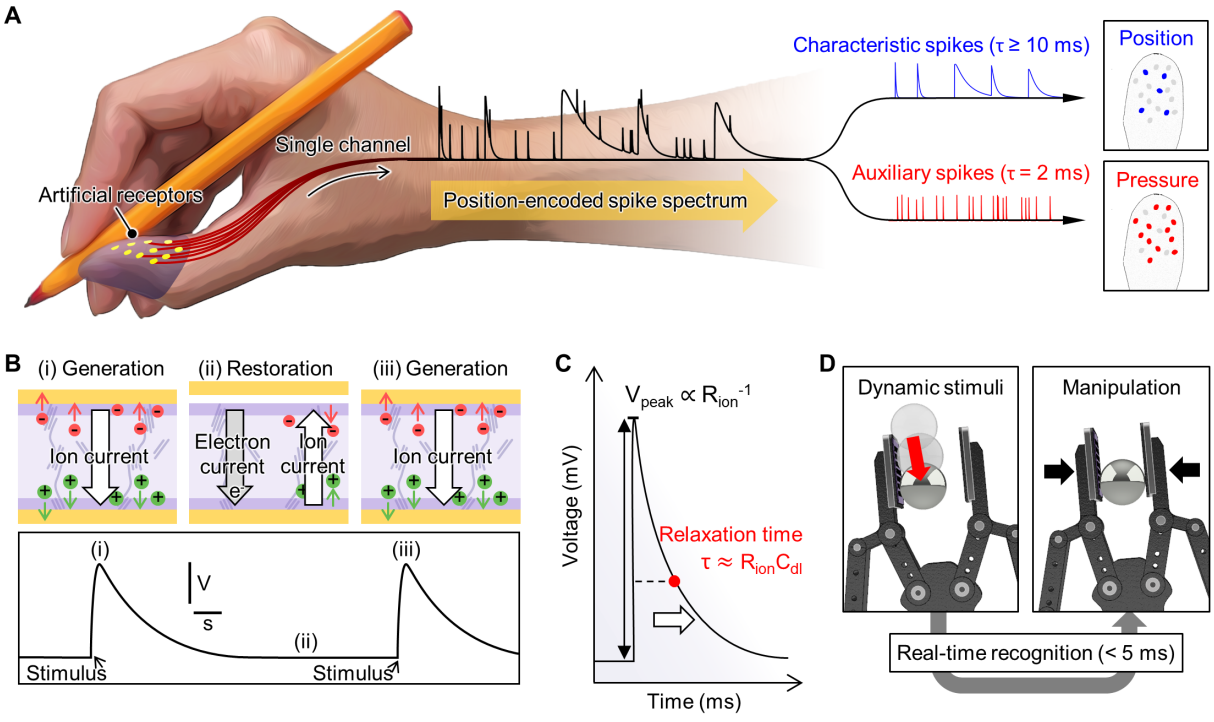

Fig. 1. Concept of the PESS. (**A**) Scheme of the artificial receptors generating the PESS, which contains the position-encoding characteristic spikes and pressure-encoding auxiliary spikes. (**B**) Ion and electron movement during the generation and restoration of the potential spike. (**C**) Characterization of the potential spike in terms of the V_{peak} and the τ. (**D**) Scheme of the artificial sensory system mounted on a robotic arm and its real-time recognition and manipulation to prevent slip of a ball.

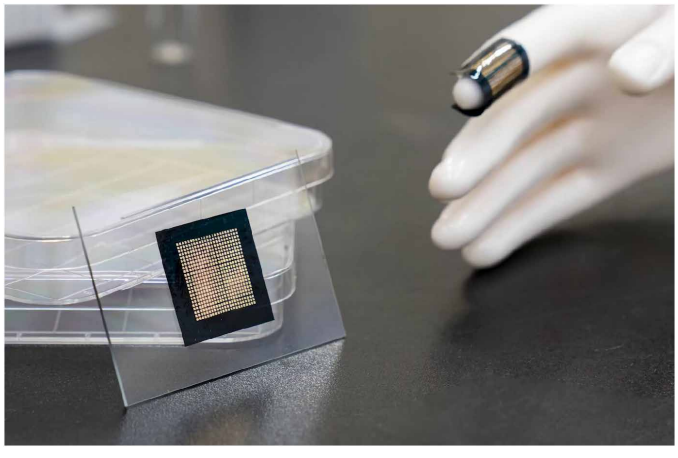

Movie 1. Overview of artificial sensory system based on the PESS.

(*24*). C_{dl} was controlled with the thickness (δ) of the PEDOT:PSS layer. R_{ion}, R_{el}, and C_{dl} were characterized by the Bode plot and the equivalent circuit model (fig. S2 and text S2).

Figure 2B shows R_{ion} and R_{el} of the MIEC layer at various ionic liquid concentration [$\phi_{ion} = w_{ion}/(w_{ion} + w_{polymer})$]. The sharp appearance of the spike was assured when $R_{ion} \ll R_{el}$ (text S1). Therefore, we fixed the PEDOT:PSS concentration [70 weight % (wt%)] with respect to PEG-DA before incorporating ionic liquid in the MIEC (fig. S3). Bode plots according to ϕ_{ion} are presented in fig. S4A. R_{ion} decreased continuously; on the other hand, R_{el} decreased rapidly in the small ϕ_{ion} because of the secondary doping effect of the ion in the PEDOT:PSS layer (*25*) and then increased gradually because of dilution of PEDOT:PSS. We used the MIEC with ϕ_{ion} = 36.4 wt% at which V_{peak} and τ could be controlled in a proper range. C_{dl} increased linearly with δ (Fig. 2C and figs. S4B and S5); meanwhile, R_{el} and R_{ion} remained unchanged because they are bulk properties of the MIEC layer.

The relaxation profiles of the spikes were distinctive according to δ (Fig. 2D). The inset is the magnification of the signals in the early stage. With increasing δ, τ increased linearly in the range of 2 to 160 ms (Fig. 2E). We set the auxiliary spike having τ = 2 ms (δ = 0) and the characteristic spikes with τ = 10 ms (δ = 50 nm), τ = 20 ms (δ = 100 nm), τ = 40 ms (δ = 200 nm), τ = 80 ms (δ = 400 nm), and τ = 160 ms (δ = 800 nm). The auxiliary spike at δ = 0 results from the C_{dl} at the interface between the Au electrode and the MIEC (fig. S4A). The average τ of the auxiliary spikes obtained from 42 different receptors was 2.0 ± 0.8 ms (fig. S6). The maximum τ of the auxiliary spike detected in the sensor was 2.5 ms, which was much smaller than that of the lowest τ (10 ms) of the characteristic spike; hence, the auxiliary spikes from any region could be decoded distinctively. V_{peak} for the characteristic spikes was the same (~56 mV) regardless of δ at the measurement frequency of 500 Hz. It is because V_{peak} depends on the bulk R_{ion} of the MIEC layer rather than the resistance near the interface with the electrode. V_{peak} for the auxiliary spike was lower (~26 mV) because the relaxation of the spike occurred too quickly to be detected (fig. S7). We confirmed that the internal closed circuit with R_{el} accelerated the discharging process in the MIEC compared with the ionic conductor gel without containing PEDOT:PSS (fig. S8). It is notable that τ and V_{peak} were dependent considerably on the measurement resistance (R_m). We fixed R_m at R_{ion}/10 on the basis of the equivalent circuit simulation (fig. S9 and text S3) because the condition caused negligible

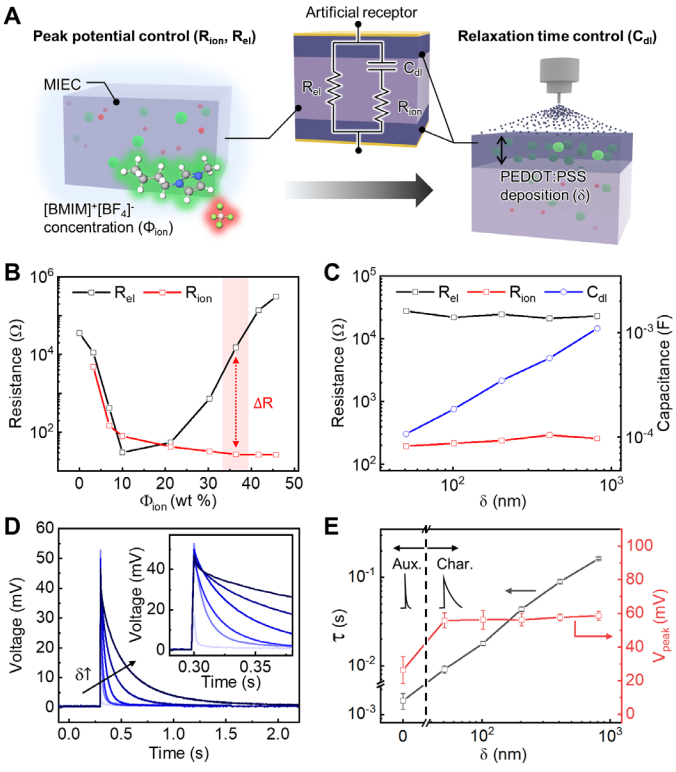

Fig. 2. Electrical characterization of the artificial receptor and its spike profile. (**A**) Controlling V_{peak} (left) and τ (right) of the unit artificial receptor. V_{peak} was controlled with the R_{ion} and R_{el}; τ was controlled with the electrical C_{dl} of the MIEC. (**B**) Changes in the R_{el} and R_{ion} of the MIEC as a function of the ionic liquid concentration (Φ_{ion}). (**C**) R_{el}, R_{ion}, and C_{dl} of the MIEC according to the δ of the PEDOT:PSS layer. (**D**) Spike profiles with different δ and their magnified profiles in the inset. (**E**) Dependence of τ and V_{peak} of the spikes according to δ. Each parameter was extracted by fitting the spike profile (D) with an exponential decay function [$V = V_{peak} \cdot \exp(-t/\tau)$].

variation in τ regardless of the number of activated spikes on the sensory system.

Spatiotemporal recognition by the PESS

We fabricated a high-resolution artificial sensory system (529 artificial receptors in 2 cm by 2 cm) (Fig. 3A). The MIEC layer was attached on the Au bottom global electrode, which had been evaporated on a poly(ethylene terephthalate) (PET) substrate. For the characteristic receptors, PEDOT:PSS patterns (0.5 mm by 0.5 mm) with various δ were obtained by spray-coating on the selected positions of the MIEC layer through a PET stencil mask with square holes. The PEDOT:PSS patterns on the top and bottom of the MIEC layer were symmetric. A PET stencil with holes arranged in a 23-by-23 square pattern was aligned on the PEDOT:PSS patterns on the MIEC film, and Au (60 nm) was sputtered through the stencil (inset in Fig. 3A). After peeling off the stencil, a new stencil with the same pattern was aligned on the Au pattern and used as the separating layer. Because of the viscoelasticity of the MIEC layer, the PET stencil was adhered directly to the MIEC layer. A stretchable Ag flake composite with a thermoplastic block copolymer, polystyrene-*block*-polybutadiene-*block*-polystyrene (SBS), was coated on a polydimethylsiloxane (PDMS) substrate (*26*). A thin Au film was sputtered on the Ag flake composite. The Au/Ag composite hybrid electrode was adhered to the PET stencil by using a double-sided tape at the edge of the sensor. The sensory system was stable under repeated bending and mechanical stimuli (pressing and shearing).

A decoder for real-time data acquisition and interpretation was developed to infer the tactile information from the PESS (Fig. 3B). The pseudo code is provided in text S4. The decoder read the PESS every 2 ms and detected a sharp potential increase to mark the occurrence of the spike. Upon detecting a spike, the decoder calculated the τ by fitting the two potential points at the spike onset with an exponential decay function. Although τ of the characteristic receptors ranged from 10 to 160 ms, the decoding time to analyze the individual spikes was the same (2 ms) regardless of τ. The fast decoding successfully identified the type of receptors from the known τ values of the characteristic and auxiliary spikes. The decoder yielded an afferent message and inferred the tactile information on the basis of the temporal arrangement of the characteristic spikes and the firing frequency of the auxiliary spikes.

The spikes were generated when the top global electrode was deformed by external force and made contacts to the Au pattern or the MIEC layer through the square hole in the separating stencil layer. When the separating stencil was thick or the hole size was small, large deformation of the top global electrode was necessary; thus, the sensitivity of the sensory system was dependent on the hole size (d_m) and the thickness (t_m) of the separating stencil, as well as on the modulus (E) of the pressing object (Fig. 3C). Figure 3D exhibits the number of spikes in the PESS when the sensory system was pressed dynamically on a flat table with a relatively hard spherical object (diameter, 25 mm; E = 600 kPa). The overall number of spikes increased with external force. The sensitivity ($S \equiv$ the number of spikes per force) increased by decreasing d_m ($S = 1.6\ N^{-1}$ at $d_m = 2.0$ mm, $S = 4.6\ N^{-1}$ at $d_m = 1.0$ mm, and $S = 8.4\ N^{-1}$ at $d_m = 0.5$ mm) due to the increased density of the artificial receptors. However, weak force was not properly sensed at $d_m = 0.5$ mm. When a soft spherical object (diameter, 25 mm; E = 55 kPa) pressed the sensor dynamically, the sensory system could not sense weak force (<2.3 N) at $d_m = 1.0$ mm; meanwhile, it showed a good linearity in the entire force range at $d_m = 2.0$ mm (Fig. 3E). We further assessed the sensing performance in terms of the sensing efficiency ($\eta \equiv$ number of activated receptor/number of pressed receptors) for different d_m and t_m (fig. S10). As d_m decreased, η decreased notably from 1 to 0.40 for hard objects and from 1 to 0 for soft objects. A dimensional condition ($d_m = 2$ mm, $t_m = 50$ μm) showed the highest η for sensing both the soft and hard objects; hence, we used these parameters for device fabrication.

The contact area information can be converted to pressure by the number of the spikes when rounded soft objects are used. In this case, the measurable pressure range was 1.5 to 10.5 kPa, and the pressure sensitivity was 2.2 kPa^{-1}, which is comparable with the sensitivity of the capacitive pressure sensor using the pyramidal elastic dielectric layer (0.2 to 0.7 kPa^{-1}) (*8*, *27*, *28*). The pressure range corresponds to the gentle touch sensed by human mechanoreceptors (<10 kPa) (*29*). The contact area information could be qualitatively obtained even when pressed using a hard cubic at relatively slow (80 kPa/s, 0.1 mm/s) and fast (280 kPa/s, 0.3 mm/s) speeds (fig. S11). Some signals were overlapped, but they could be decoded to provide the spatiotemporal change of the contact area. This is because the contacts do not take place in the exactly concurrent manner over the whole surface area even when two flat surfaces are in contact (*30*). In addition, τ of the auxiliary spikes does not change, and V_{peak} increases linearly with increasing number of overlaps (fig. S12);

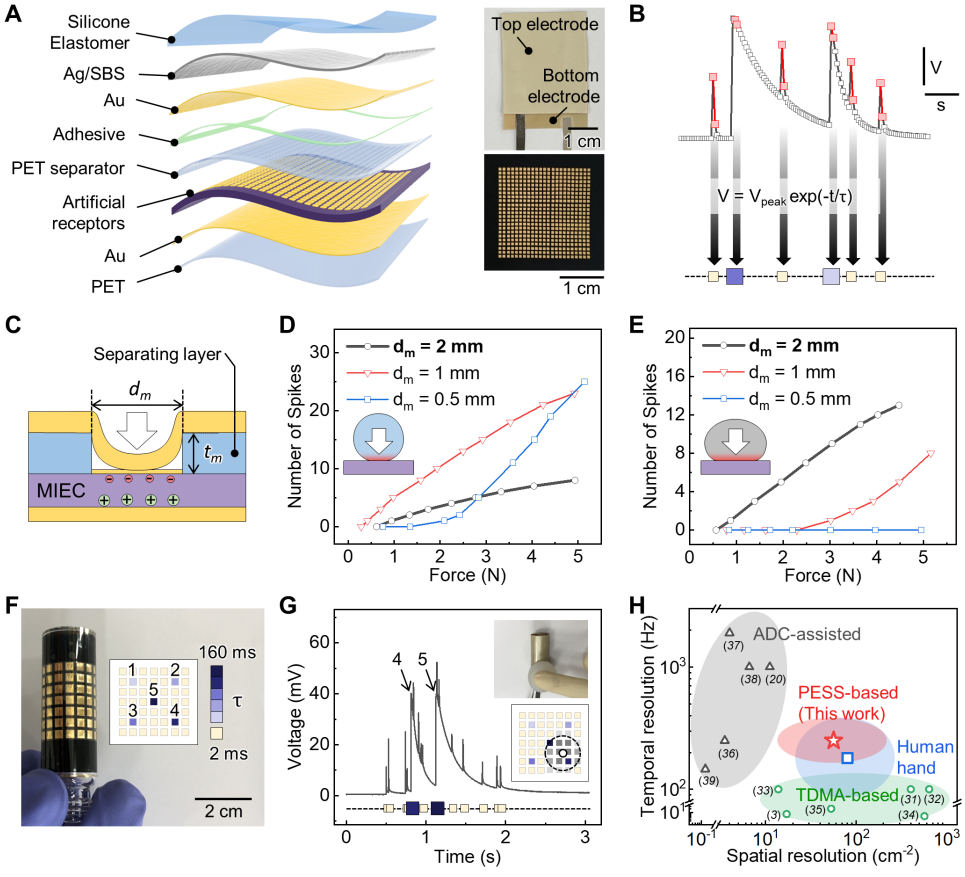

Fig. 3. Structure of the artificial sensory system and PESS decoding process to infer the normal force stimuli. (**A**) Structural design and camera images of the artificial sensory system. The system contains 23-by-23 auxiliary receptors in 2 cm by 2 cm. The characteristic receptors have PEDOT:PSS patterns on the MIEC layer. All the receptors have the Au patterns. The top surface of the MIEC layer has a separating layer with square holes. The receptors share the top and bottom global electrodes. (**B**) Real-time decoding of the PESS. τ values are extracted by two-point exponential fitting for each spike in PESS. (**C**) Dimensional description of the separating layer with respect to the square hole size (d_m) and the thickness (t_m). The global top electrode makes contact to the Au pattern through the square holes. (**D** and **E**) Dependence of the number of spikes on d_m when pressed with hard (D) and soft (E) spherical objects at various normal forces. (**F**) Camera image of a flexible artificial sensory system wrapped on a small vial. The characteristic receptors are numbered in the order of increasing τ. The global top electrode is not covered to show the array of the receptors. The five characteristic receptors are numbered in the inset. (**G**) PESS from the sensory system when pressed at arbitrary position. The camera images of the pressing motion and the inferred information (position and area) are shown in the inset. (**H**) Spatial and temporal resolutions of the PESS-based sensory system (this work) compared with the FA-I afferent of human hand and the reported artificial sensors (ADC-assisted, TDMA-based sensors).

hence, the overlapped auxiliary spikes can be decoded. With a bent surface either from the contact object or the sensor, the contacts are more localized and changes dynamically, which makes the exact concurrent contacts less probable. Machine learning–based decoding is expected to decipher the PESS generated by objects with more complicated shapes.

The sensory system was flexible because all the materials were highly flexible or stretchable (Fig. 3F). The resistance of the electrode and the capacitance of the device were unchanged in the bending radius of larger than 8 mm; therefore, the changes in V_{peak} and τ by bending were negligible (fig. S13), and decoding of the PESS was possible without an additional calibration process. The camera image was taken without the global top electrode to show the receptors of the sensory system. The characteristic receptors are numbered in the order of increasing τ. Figure 3G (also movie S1) shows the PESS and real-time decoding to obtain dynamic pressure distribution. The sensory system (inset camera image) wrapping around a vial is silver-colored because of the Ag flake composite global top electrode. When force was applied with a soft spherical object between nos. 5 and 4 receptors, the auxiliary spikes appeared first and then the characteristic spikes appeared in sequence along with the auxiliary spikes. In addition to the initial contact points and the final contact area, the decoding provides the dynamic information of the contact spreading rates (73 mm^2/s). The accuracy of estimating the contact area (number of spikes) and position (relative timing of the characteristic spikes) was very high (fig. S14). The total number of spikes was nearly the same (13 to 14 spikes) during 19 repeated stimuli, and the statistical deviation in the relative timing of the characteristic spikes from the initial spike was less than 1%. Pressing other parts on the sensory system showed a similar PESS behavior (fig. S15). These results open the possibility of omnidirectional tactile perception.

Spatiotemporal resolution of the PESS sensory system

In the biological afferent sensory system, the FA-I afferent in the hand innervates at least 20 Meissner corpuscles (*31*). The first spikes from the afferents are selectively used for fast temporal perception (30 to 250 Hz) (*22*, *32*, *33*), and a large number of afferents are required for high spatial resolution (141/cm^2 in the fingertip and 25/cm^2 in the palm) (*17*, *31*). In this study, the introduction of the characteristic spikes among the auxiliary spikes made it possible to emulate similar levels of spatial (12 to 132/cm^2) and temporal (≤250 Hz) resolutions (Fig. 3H). In addition, the sensory system requires only two signal addressing lines even for a number of the artificial receptors (fig. S16). The high spatiotemporal resolution and the structural simplicity of our sensory system are advantageous over the TDMA-based and ADC-assisted tactile sensors. The TDMA-based E-skins achieved a high density of pixels by the multiplexed electrode array; however, their temporal resolution was limited up to 100 Hz (*3*, *34*–*38*). Because the number of addressing lines increased with the number of the pixels in the TDMA-based sensors, achieving a high temporal resolution simultaneously with a high spatial resolution is difficult. The event-driven E-skins using the ADCs could engineer the spike frequency in a high temporal resolution (150 Hz to 1.9 kHz) (*20*, *39*–*42*); however, each pixel in the sensing part requested an ADC, which made the structure

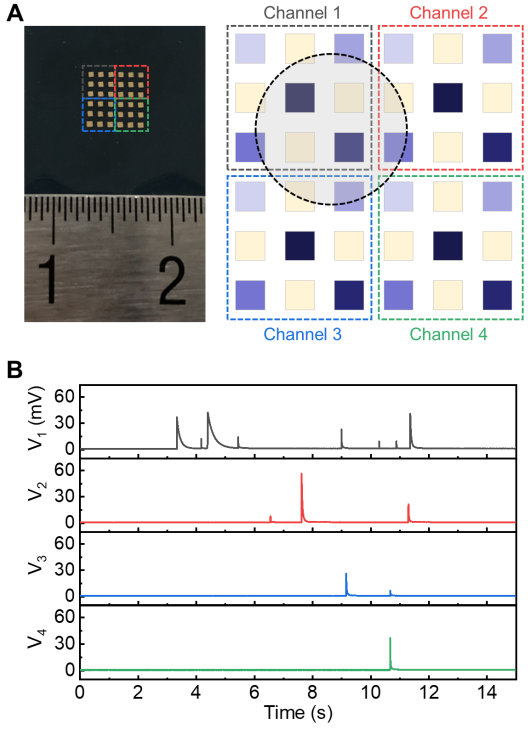

Fig. 4. Integration of multiple artificial sensory systems to enhance the spatial resolution. (**A**) Camera image and design of the artificial receptors for the sensory system with four independent sensing channels (1 to 4). The dashed circle indicates the stimulated area applied by pressing the system with a rigid spherical object (diameter, 25 mm). (**B**) The PESSs from the four sensing channels (V_1 to V_4).

complicated and reduced the spatial resolution. Because the sensory system in this study does not request the ADC in the sensing part, the spatial resolution could be considerably improved. The one ADC used in this study was for data storage and computational process, which is essential in any sensing system.

The spatial resolution is determined by the spatial density of the characteristic receptors when the contact object is stationary. Similar to the characteristic spikes, the auxiliary spikes can be used to obtain the relative position information over time along the trajectory provided by the characteristic spikes when the object is moving dynamically. By using the same five characteristic receptors, the spatial resolution for a stationary object can be considerably enhanced by integrating multiple PESS sensors and designing the distribution of the receptors as illustrated in Fig. 4A. This integration contains four separated sensing systems, which requires four sensing channels for measurement. Because the four sensors share the same MIEC film, the fabrication process is simple and requests only the separated pairs of top and bottom global electrodes. With the same size of the receptors (0.5 mm by 0.5 mm), this design can increase the stationary spatial resolution to 80/cm^2 and the dynamic spatial resolution to 132/cm^2. Figure 4B exhibits the PESS from the four channels when a spherical object (diameter, 25 mm) was pressed on the integrated system. Because the distance between two characteristic receptors was the same or less than 1 mm, any object making the contact area larger than 1 mm should contain more than one characteristic spike together with the auxiliary spikes. This is a sufficient spatial resolution for analyzing most dynamic stimuli applied on the sensory system.

Two-dimensional stimuli detection

Two-dimensional drawing motions were applied on the single sensory system to exhibit the dynamic tactility. Figure 5A (also in movie S2) shows the letter "Z" drawn at a speed of 5 mm/s under different forces (1.3 and 1.6 N) and the corresponding PESS. The motion trace and the drawing speed were decoded from the sequence of the characteristic spikes. The contact area by the pressing object was analyzed by the number of the auxiliary spikes, drawing along a single row (marked by a black dotted trace) and along three rows (marked by a red dotted trace). Decoding of the slip angle is essential in perception of dynamic mechanical stimuli. Figure 5B exhibits slip motion with a cylindrical bar at different angles ($\theta = 30°$, 60°, and 180°) and a slip speed of 5 mm/s. The corresponding PESSs are shown in the figure. The 12 PESSs obtained at every 30° are compared in fig. S17. When the angle matches with the column ($\theta = 0°$ and 180°) or the row ($\theta = 90°$ and 270°), the spikes were overlapped but could be identified by peak deconvolution (fig. S18). The sequence of the characteristic spikes and the relative timing between the characteristic spikes was used to distinguish the angle. On the basis of the information of the sensory system (τ, d_m, device area, and density of the receptors), we developed a simulator that generated a synthetic PESS upon virtual stimulation on a computer screen (MATLAB R2020a, MathWorks Inc.). The results from simulated PESS were in agreement with the results from experimental PESS (movie S3), demonstrating the possibility to simulate the PESS in response to virtual dynamic tactility.

When the slip angle was small, delicate angle information was obtained from the spike frequency (ν) in the PESS (Fig. 5C). The effective distance (Δd) between the neighboring receptors, thus also the temporal spacing (Δt) between the neighboring spikes, varied with the slip angle. Figure 5D compares the PESS at the small slip angles ($\theta = 0°$, 2°, and 6°) at 5 mm/s. The spikes from the same column or row appeared in bundles when $\theta < 8°$ but not when $\theta \geq 8°$ (fig. S19). ν was calculated by dividing the number of spikes by a given time period ($\zeta = 160$ ms). The maximum spike frequency (ν_{max}) of each spike bundle was obtained from the histogram (Fig. 5E), and the average ν_{max} ($<\nu_{max}>$) from the seven bundles was calculated. $<\nu_{max}>$ decreased as θ increased because Δd in the same column or row increased. We found that the slip speed and slip angle could be simultaneously measured because both could be decoded using the sequence and the relative timing of the characteristic spikes (fig. S20).

Real-time robotic feedback

We integrated the artificial sensory system on a robotic arm to implement a real-time dynamic tactile feedback system (Fig. 6A). Figure 6B (also see movie S4) shows a series of object manipulation. The robotic arm grasped a spherical metal ball (3 cm in diameter) placed on a table. The initial grasping point was at the tip of the gripper, recognizing the position and contact area of the ball through the real-time decoding of the PESS. The arm rotated up and released the grip to allow the ball to fall down. The gripper closed instantaneously when the ball reached the bottom of the grip. The arm rotated down and was shaken rapidly. The sensory system could prevent sudden slip of the ball because the grip was tightened dynamically when slight slip was detected. It is notable that the

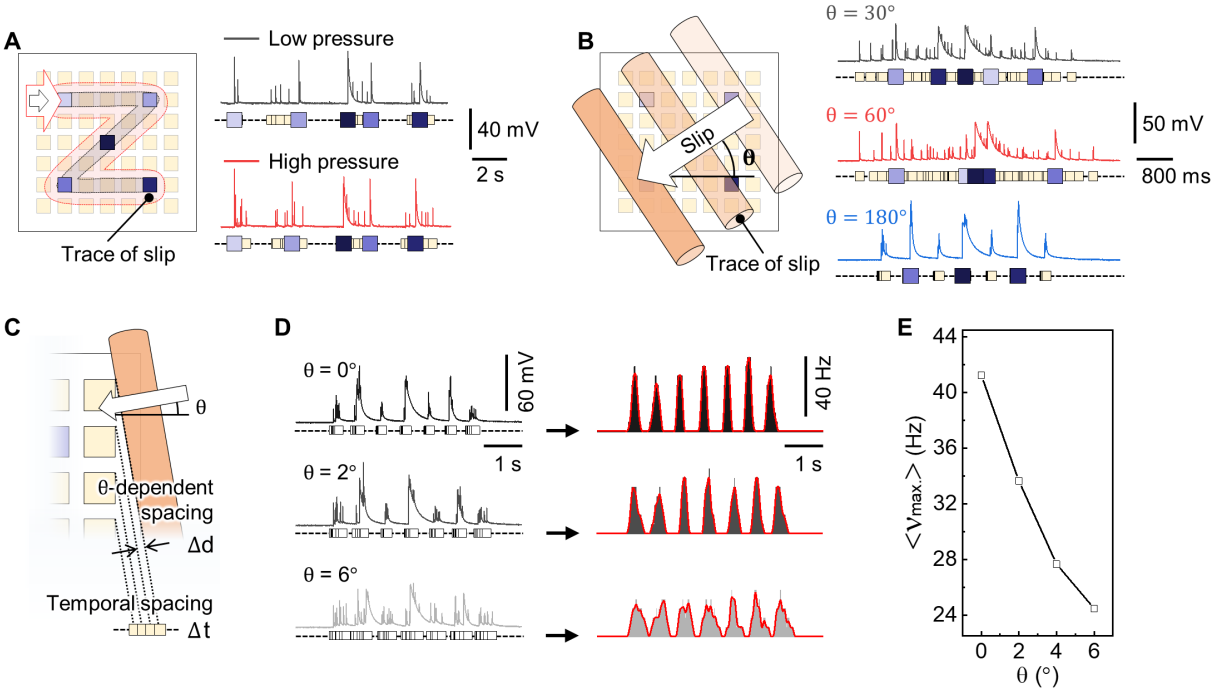

Fig. 5. Dynamic tactility of the artificial sensory system in response to two-dimensional motions. (**A**) Scheme of the slip-and-drawing stimulation (left). Black and red shaded areas indicate the different traces of the stimulated contact area by applying low pressure (black) and high pressure (red). Corresponding PESS were described (right). (**B**) Scheme of a slip with a cylindrical object at different large slip angles (θ) and the PESS measured at θ = 30°, 60°, and 180°. (**C** to **E**) Delicate slip angle analysis at small slip angles (θ ≤ 8°). (C) Scheme of a slip with a cylindrical object at a small slip angle. The spatial spacing (Δ*d*) and the temporal spacing (Δ*t*) between the receptors are sensitive to the slip angle. (D) PESS measured at θ = 0°, 2°, and 6°. The firing frequency (ν) of the collective spike bundles are presented with red lines. (E) Averaged maximum ν (<ν_{max}>) from the bundles according to θ.

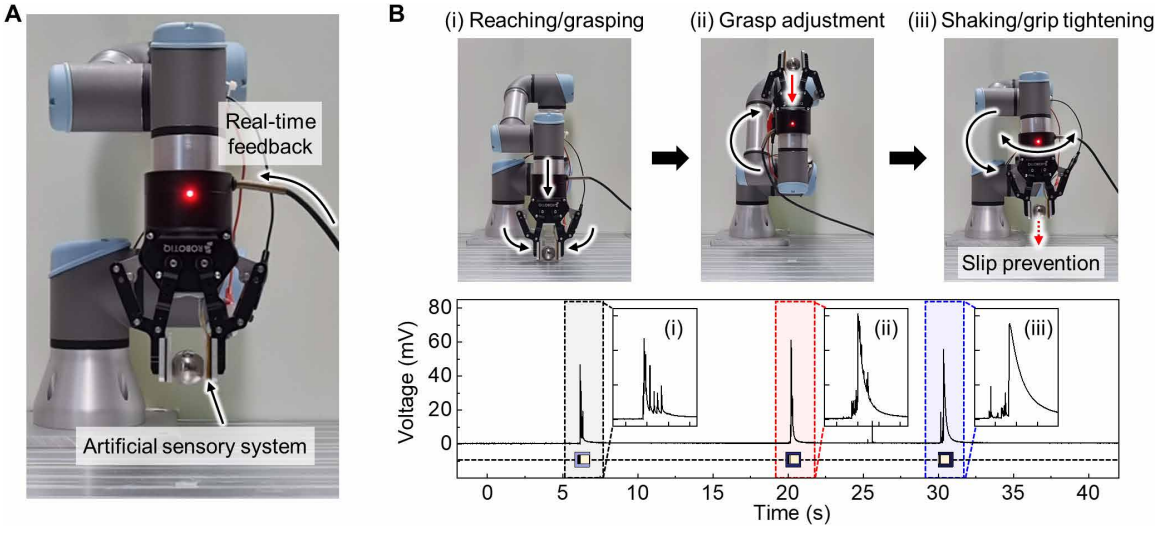

Fig. 6. Real-time dynamic robotic grasp control based on the tactile feedback. (**A**) Camera image of the robotic arm holding a metal ball with the artificial sensory system. (**B**) Camera images of the robotic arm during a series of object manipulation (grasping, rotation, falling of the ball and tightening the grip, and slip prevention during rapid shaking). The black and red arrows represent the movement of the robotic arm and the falling of the ball, respectively. The corresponding PESS are shown below.

shaking motion caused immediate falling of the ball without using the sensor system (see the end of movie S4).

The accuracy of robot arm manipulation should not be affected by object temperature or environmental temperature. We found that V_{peak} increased with increasing temperature in the range of 25° to 50°C, whereas τ decreased on both auxiliary spike and characteristic spikes (fig. S21). Because temperature can be calculated from the measured ion charge τ when the environment temperature changes or the object temperature changes (*2*), τ and V_{peak} for each receptor can be calibrated and used for decoding the spike profiles.

DISCUSSION

There are four main factors with regard to the maximum number of receptors that can be analyzed in real time in a single sensory system. First, the time required for the pattern analysis does not increase with the number of the receptors because the spike information of all artificial receptors is collected in parallel. Therefore, the number of receptors for real-time analysis is, in principle, not limited if the measurement is fast enough. Second, the time of data measurement cycle (Δt_m) of the equipment versus the time difference between two spikes (Δt_p) affects the minimum time required for pattern analysis. When $\Delta t_m \leq \Delta t_p$, each spike can be identified successfully because of the sufficient number of data points for the two-point decoding. Because Δt_m was 2 ms in our measurement setup and τ of the auxiliary spikes was 2.0 ms, all the spikes could be analyzed. With a smaller Δt_m, for instance, Δt_m = 0.2 ms, the auxiliary spikes with a much smaller τ can be analyzed so that the maximum number of the receptors for real-time analysis increases (fig. S22). On the contrary, when $\Delta t_m > \Delta t_p$, the decoder requires four to five data points (~10 ms) to identify each τ when the spikes are overlapped. Third, the thickness, dimension of the hole in the separating stencil layer, and its modulus limit the sensor resolution. A thinner and softer stencil layer allows the contact of the top global electrode through a smaller hole dimension so that the detectable spatial resolution and sensitivity can be increased. Although the maximum number of the auxiliary receptors in the single sensory system was 132/cm^2 in this study (fig. S23), the number of receptors could be increased through improvement in measurement equipment and the stencil layer. Fourth, the number of the distinguished characteristic spikes depends on the reliable control over the thickness of the PEDOT:PSS layer because τ of the characteristic receptors are controlled by the thickness. The τ values obtained by the exponential curve fitting had a negligible calculation error (<0.2%). For instance, the average τ of the characteristic receptor no. 4 was 107.5 ms, and the maximum deviation was 0.2 ms during 500 pressing cycles (fig. S24). This robustness indicates that the property of the PEDOT:PSS does not change once the ionic molecules are incorporated in the layer, therefore maintaining constant V_{peak} and τ. Unfortunately, delicate thickness control of the PEDOT:PSS coating on the target positions for the characteristic receptors was not achieved yet in this study. That was the reason why we distinguished only five characteristic spikes and decreased the spatial resolution for real-time decoding. Advanced coating process will allow fine control of τ and increase the decodable spatial resolution.

Although this study focuses on the rectangular array of the square-type receptors, fabrication of complex curved receptors and their arbitrary distribution are enabled simply by preparing the PEDOT:PSS pattern and the Au pattern through a mask with the complex design (fig. S25). The complexity in the receptor shape and their distribution is an interesting fundamental issue for understanding the efficacy of human receptors.

In summary, we proposed an artificial sensory system for dynamic tactile perception. A temporal sequence of the spikes generated in the artificial receptors, called PESS, consists of the characteristic spikes containing the position information and the auxiliary spikes presenting the speed and contact area of the tactile stimulation. With a pattern decoding algorithm, this event-driven PESS allows a high spatiotemporal resolution of the fast-adapting afferent and enables us to perceive complicated dynamic tactile motions. This simple-structured sensing system is expected to pave the possibility of a high-resolution omnidirectional artificial skin that can be used for service robots and for understanding/restoring the sensation of human skin.

MATERIALS AND METHODS

Preparation of the MIEC film

2-hydroxy-2-methylpropiophenone (0.02 ml; Sigma-Aldrich) was added in PEG-DA (M_n = 575; 0.98 ml; Sigma-Aldrich). An aqueous solution of PEDOT:PSS (2.33 ml; product: Clevios P, Heraeus) was filtered using a 5-μm polytetrafluoroethylene filter (product: WHA67841350, Merck), and it was added in the PEG-DA prepolymer solution (1.00 ml). The weight ratio between the PEDOT:PSS solution and the prepolymer solution was 7:3. The mixture solution was injected between two slide glasses with a spacing gap of 180 μm and then exposed to ultraviolet light (λ = 365 nm, 48 mW, 10 s) for photopolymerization. The cured PEDOT:PSS/PEG-DA gel film was dried at 80°C for 2 hours and further dried in vacuum at room temperature for 4 hours to remove residual water in the gel film. After drying, the gel film was dipped in an aqueous ionic liquid solution of BMIM:BF_4 (20 wt% in water; Sigma-Aldrich) for 24 hours. The mixed ion-electron gel was dried at 80°C for 2 hours and further dried in vacuum for 4 hours at room temperature. The dried gel film was used as the MIEC in this study.

Fabrication procedure of the artificial sensory system

A 50-μm-thick PET stencil mask was prepared using a razor cutter (model CE6000-40, Graphtec). The stencil mask had five square-patterned holes with different hole sizes (d_m = 0.5, 1, 2, and 8 mm). Those locations corresponding to the holes were the characteristic pixels. The MIEC film was placed on a polytetrafluoroethylene (Teflon) film, and the five-hole PET stencil was placed on the top surface of the MIEC film. The aqueous PEDOT:PSS solution was diluted from 5 to 100 times to accurately control the amount of PEDOT:PSS. At 120°C, the diluted PEDOT:PSS solution was spray-coated through the five-hole PET stencil. The same diluted PEDOT:PSS solution was also spray-coated on the bottom surface of the MIEC film. The thickness of the spray-coated PEDOT:PSS pattern (δ = 0, 50, 100, 200, 400, and 800 nm) was adjusted by the degree of dilution and the spraying time. To form δ = 50 nm, 2.76 ml of 100 times diluted PEDOT:PSS aqueous solution was sprayed on the MIEC. To form δ = 100 nm and δ = 200 nm, 1.11 and 2.22 ml of 20 times diluted PEDOT:PSS aqueous solution was sprayed on the MIEC. δ = 100 nm and δ = 200 nm were obtained by spraying 1.11 and 2.22 ml of five times diluted PEDOT:PSS aqueous solution. To make the PEDOT:PSS patterns symmetric on the top and bottom surfaces, the position of the five-hole PET stencil was aligned using a mask aligner. Another PET stencil having the periodic square holes (7 × 7, 15 × 15, 23 × 23 holes) on the entire area was prepared using a Graphtec razor cutter. The periodic PET stencil was placed on the top surface of the MIEC film with the PEDOT:PSS patterns. The stencil was aligned for the PEDOT:PSS patterns that were matched with the stencil holes. Au (60 nm) was sputtered through the periodic stencil. After peeling off the stencil, the same but new stencil was placed on Au pattern and used as the separating layer.

For the bottom global electrode, Au was sputtered on a 50-μm-thick PET film. For the top global electrode, a stretchable Ag flake composite modified by sputtered Au film was used. Silver flake (product: 47MR-12F, Inframat Advanced Materials LLC, USA) was added to

a solution of SBS (M_w = 140,000; Sigma-Aldrich; 10 wt% in chloroform). The weight ratio of the Ag flake and the polymer solution was 1:2. The silver flake/SBS blend was spin-coated (1000 rpm, 30 s) on a Si wafer. After annealing at 80°C for 30 min, the composite film was treated by O_2 plasma [100 W; plasma time, 60 s; and O_2 gas flow rate, 22 standard cc per minute (sccm)]. The PDMS (SYLGARD 184, Dow Corning) prepolymer solution (30:1 ratio between the prepolymer and the curing agent) was spin-coated (150 rpm, 60 s) on the Ag/SBS composite electrode. The 60-μm-thick PDMS was cured at 80°C for 6 hours. To reduce the stickiness of the PDMS and make handling easier, silica particle powder (or baby powder) was rubbed on the side of the PDMS layer. Au was sputtered on the Ag flake/SBS composite electrode. The MIEC with the Au pattern was placed on the common bottom electrode and covered with the separating layer (periodic stencil). Then, the top global electrode was attached to the edges of the separating layer using a double-sided tape (3M).

Impedance measurement

Au (8 mm by 8 mm) was sputtered on two PET substrates, and they were attached to the top and bottom sides of the MIEC film. Conductive tapes (product: ST-610, Daehyun ST, South Korea) were connected to the top and bottom global electrodes. Impedance spectroscopy was measured using an impedance analyzer (model PalmSense4, PalmSense, The Netherlands). AC potential (50 mV) was applied to measure impedance with the frequency range of 0.01 Hz to 1.0 MHz.

Measurement of the PESS

Conductive tapes were connected to the top and bottom global electrodes of the artificial sensory system. The two metal wires were connected using a voltage source at 0.8 V (function generator; model 33220A, Keysight, USA), and the external R_m was set to be 10 times less than R_{ion}, $R_m = (1/10)R_{ion}$. The potential spike profiles were measured at the measurement frequency of 500 Hz. Controlled pressure and slip were applied to the artificial sensory system by using a universal measurement probe (Teraleader Co., South Korea). The single spike and spike train profiles were measured with open circuit potentiometry (model PalmSense4, PalmSense, The Netherlands). Ion restoration behavior was examined by measuring the open circuit potential of the MIEC film after applying 0.8-V DC bias.

Circuit simulation

Simulink (MATLAB R2020a, MathWorks Inc., Natick, MA, USA) was used to simulate the PESS. The electrical circuit was constructed on Simulink in the same way as the experimental setup. The values of the circuit elements were set as experimentally measured parameters. The data were acquired at 500-Hz measurement frequency. The τ of the simulated spikes was analyzed by curve fitting with the exponential governing equation ($y = y_0 + A \cdot e^{-x/\tau}$).

Real-time robotic grasp control

The robotic arm (UR3, Universal Robots, Denmark) and the gripper (2F-85, Robotiq, Canada) were controlled using Python and MATLAB through Transmission Control Protocol/Internet Protocol (TCP/IP) communication. The artificial sensory system was attached to one side of the gripper. During the object manipulation, the PESS were collected using PalmSens4 and decoded using MATLAB at real time. The gripper was operated in response to the PESS to perform real-time grasp control based on tactile feedback.

SUPPLEMENTARY MATERIALS

www.science.org/doi/10.1126/scirobotics.abl5761
Text S1 to S4
Figs. S1 to S25
Movies S1 to S4

REFERENCES AND NOTES

1. T. Someya, M. Amagai, Toward a new generation of smart skins. *Nat. Biotechnol.* **37**, 382–388 (2019).
2. I. You, D. G. Mackanic, N. Matsuhisa, J. Kang, J. Kwon, L. Beker, J. Mun, W. Suh, T. Y. Kim, J. B.-H. Tok, Z. Bao, U. Jeong, Artificial multimodal receptors based on ion relaxation dynamics. *Science* **370**, 961–965 (2020).
3. S. Sundaram, P. Kellnhofer, Y. Li, J.-Y. Zhu, A. Torralba, W. Matusik, Learning the signatures of the human grasp using a scalable tactile glove. *Nature* **569**, 698–702 (2019).
4. T. Yokota, T. Nakamura, H. Kato, M. Mochizuki, M. Tada, M. Uchida, S. Lee, M. Koizumi, W. Yukita, A. Takimoto, T. Someya, A conformable imager for biometric authentication and vital sign measurement. *Nat. Electron.* **3**, 113–121 (2020).
5. H. U. Chung, B. H. Kim, J. Y. Lee, J. Lee, Z. Xie, E. M. Ibler, K. Lee, A. Banks, J. Y. Jeong, J. Kim, C. Ogle, D. Grande, Y. Yu, H. Jang, P. Assem, D. Ryu, J. W. Kwak, M. Namkoong, J. B. Park, Y. Lee, D. H. Kim, A. Ryu, J. Jeong, K. You, B. Ji, Z. Liu, Q. Huo, X. Feng, Y. Deng, Y. Xu, K.-I. Jang, J. Kim, Y. Zhang, R. Ghaffari, C. M. Rand, M. Schau, A. Hamvas, D. E. Weese-Mayer, Y. Huang, S. M. Lee, C. H. Lee, N. R. Shanbhag, A. S. Paller, S. Xu, J. A. Rogers, Binodal, wireless epidermal electronic systems with in-sensor analytics for neonatal intensive care. *Science* **363**, eaau0780 (2019).
6. Y. Liu, J. Li, S. Song, J. Kang, Y. Tsao, S. Chen, V. Mottini, K. McConnell, W. Xu, Y.-Q. Zheng, J. B.-H. Tok, P. M. George, Z. Bao, Morphing electronics enable neuromodulation in growing tissue. *Nat. Biotechnol.* **38**, 1031–1036 (2020).
7. H. van Hoof, T. Hermans, G. Neumann, J. Peters, Learning robot in-hand manipulation with tactile features, in *Proceedings of the IEEE-RAS 15th International Conference on Humanoid Robots (Humanoids)* (IEEE, 2015), pp. 121–127.
8. C. M. Boutry, M. Negre, M. Jorda, O. Vardoulis, A. Chortos, O. Khatib, Z. Bao, A hierarchically patterned, bioinspired e-skin able to detect the direction of applied pressure for robotics. *Sci. Robot.* **3**, eaau6914 (2018).
9. E. D'Anna, G. Valle, A. Mazzoni, I. Strauss, F. Iberite, J. Patton, F. M. Petrini, S. Raspopovic, G. Granata, R. Di Iorio, M. Controzzi, C. Cipriani, T. Stieglitz, P. M. Rossini, S. Micera, A closed-loop hand prosthesis with simultaneous intraneural tactile and position feedback. *Sci. Robot.* **4**, eaau8892 (2019).
10. M. A. Schiefer, E. L. Graczyk, S. M. Sidik, D. W. Tan, D. J. Tyler, Artificial tactile and proprioceptive feedback improves performance and confidence on object identification tasks. *PLOS ONE* **13**, e0207659 (2018).
11. D. D. Falconer, F. Adachi, B. Gudmundson, Time division multiple access methods for wireless personal communications. *IEEE Commun. Mag.* **33**, 50–57 (1995).
12. J.-F. Wu, Scanning approaches of 2-D resistive sensor arrays: A Review. *IEEE Sens. J.* **17**, 914–925 (2017).
13. Ó. Oballe-Peinado, J. A. Hidalgo-López, J. A. Sánchez-Durán, J. Castellanos-Ramos, F. Vidal-Verdú, Architecture of a tactile sensor suite for artificial hands based on FPGAs, in *Proceedings of the IEEE RAS & EMBS Internatinal Conference on Biomedical Robotics Biomechatronics (BioRob)*, (IEEE, 2012), pp.112–117.
14. P. A. Schmidt, E. Maël, R. P. Würtz, A sensor for dynamic tactile information with applications in human–robot interaction and object exploration. *Rob. Auton. Syst.* **54**, 1005–1014 (2006).
15. S. M. Won, H. Kim, N. Lu, D. Kim, C. Del Solar, T. Duenas, A. Ameen, J. A. Rogers, Piezoresistive strain sensors and multiplexed arrays using assemblies of single-crystalline silicon nanoribbons on plastic substrates. *IEEE Trans. Electron Devices* **58**, 4074–4078 (2011).
16. K. Weiss, H. Worn, Resistive tactile sensor matrices using inter-electrode sampling, in *Proceedings of the 31st Annual Conference of IEEE Industrial Electronics Society, 2005. IECON*, (IEEE, 2005), pp. 1949–1954.
17. R. S. Johansson, J. R. Flanagan, Coding and use of tactile signals from the fingertips in object manipulation tasks. *Nat. Rev. Neurosci.* **10**, 345–359 (2009).
18. B. C.-K. Tee, A. Chortos, A. Berndt, A. K. Nguyen, A. Tom, A. McGuire, Z. C. Lin, K. Tien, W.-G. Bae, H. Wang, P. Mei, H.-H. Chou, B. Cui, K. Deisseroth, T. N. Ng, Z. Bao, A skin-inspired organic digital mechanoreceptor. *Science* **350**, 313–316 (2015).
19. Y. Kim, A. Chortos, W. Xu, Y. Liu, J. Y. Oh, D. Son, J. Kang, A. M. Foudeh, C. Zhu, Y. Lee, S. Niu, J. Liu, R. Pfattner, Z. Bao, T.-W. Lee, A bioinspired flexible organic artificial afferent nerve. *Science* **360**, 998–1003 (2018).
20. W. W. Lee, Y. J. Tan, H. Yao, S. Li, H. H. See, M. Hon, K. A. Ng, B. Xiong, J. S. Ho, B. C.-K. Tee, A neuro-inspired artificial peripheral nervous system for scalable electronic skins. *Sci. Robot.* **4**, eaax2198 (2019).
21. R. S. Johansson, I. Birznieks, First spikes in ensembles of human tactile afferents code complex spatial fingertip events. *Nat. Neurosci.* **7**, 170–177 (2004).

22. H. P. Saal, S. Vijayakumar, R. S. Johansson, Information about complex fingertip parameters in individual human tactile afferent neurons. *J. Neurosci.* **29**, 8022–8031 (2009).
23. S. Panzeri, R. S. Petersen, S. R. Schultz, M. Lebedev, M. E. Diamond, The role of spike timing in the coding of stimulus location in rat somatosensory cortex. *Neuron* **29**, 769–777 (2001).
24. J. Rivnay, P. Leleux, M. Ferro, M. Sessolo, A. Williamson, D. A. Koutsouras, D. Khodagholy, M. Ramuz, X. Strakosas, R. M. Owens, C. Benar, J.-M. Badier, C. Bernard, G. G. Malliaras, High-performance transistors for bioelectronics through tuning of channel thickness. *Sci. Adv.* **1**, e1400251 (2015).
25. Y. Wang, C. Zhu, R. Pfattner, H. Yan, L. Jin, S. Chen, F. Molina-Lopez, F. Lissel, J. Liu, N. I. Rabiah, Z. Chen, J. W. Chung, C. Linder, M. F. Toney, B. Murmann, Z. Bao, A highly stretchable, transparent, and conductive polymer. *Sci. Adv.* **3**, e1602076 (2017).
26. H. Roh, S. Cho, G. Lee, S. Moon, M. Kong, I. You, U. Jeong, Liquid metal covered with thermoplastic conductive composites for high electrical stability and negligible electromechanical coupling at large strains. *ACS Appl. Mater. Interfaces* **11**, 26204–26212 (2019).
27. S. C. B. Mannsfeld, B. C.-K. Tee, R. M. Stoltenberg, C. V. H.-H. Chen, S. Barman, B. V. O. Muir, A. N. Sokolov, C. Reese, Z. Bao, Highly sensitive flexible pressure sensors with microstructured rubber dielectric layers. *Nat. Mater.* **9**, 859–864 (2010).
28. Y. Zhang, Y. Fang, J. Li, Q. Zhou, Y. Xiao, K. Zhang, B. Luo, J. Zhou, B. Hu, Dual-mode electronic skin with integrated tactile sensing and visualized injury warning. *ACS Appl. Mater. Interfaces* **9**, 37493–37500 (2017).
29. E. S. Dellon, R. Mourey, A. L. Dellon, Human pressure perception values for constant and moving one- and two-point discrimination. *Plast. Reconstr. Surg.* **90**, 112–117 (1992).
30. J. H. Lee, I. Yu, S. Hyun, J. K. Kim, U. Jeong, Remarkable increase in triboelectrification by enhancing the conformable contact and adhesion energy with a film-covered pillar structure. *Nano Energy* **34**, 233–241 (2017).
31. G. Corniani, H. P. Saal, Tactile innervation densities across the whole body. *J. Neurophysiol.* **124**, 1229–1240 (2020).
32. E. L. Mackevicius, M. D. Best, H. P. Saal, S. J. Bensmaia, Millisecond precision spike timing shapes tactile perception. *J. Neurosci.* **32**, 15309–15317 (2012).
33. A. I. Weber, H. P. Saal, J. D. Lieber, J.-W. Cheng, L. R. Manfredi, J. F. Dammann, S. J. Bensmaia, Spatial and temporal codes mediate the tactile perception of natural textures. *Proc. Natl. Acad. Sci. U.S.A.* **110**, 17107–17112 (2013).
34. H. Oh, G.-C. Yi, M. Yip, S. A. Dayeh, Scalable tactile sensor arrays on flexible substrates with high spatiotemporal resolution enabling slip and grip for closed-loop robotics. *Sci. Adv.* **6**, eabd7795 (2020).
35. M. Park, M.-S. Kim, Y.-K. Park, J.-H. Ahn, Si membrane based tactile sensor with active matrix circuitry for artificial skin applications. *Appl. Phys. Lett.* **106**, 043502 (2015).
36. R. Surapaneni, Y. Xie, Q. Guo, D. J. Young, C. H. Mastrangelo, A high-resolution flexible tactile imager system based on floating comb electrodes, in *Proceedings of the 2012 IEEE SENSORS* (IEEE, 2012), pp. 208–211.
37. E. Sotgiu, D. E. Aguiam, C. Calaza, J. Rodrigues, J. Fernandes, B. Pires, E. E. Moreira, F. Alves, H. Fonseca, R. Dias, S. Martins, J. Gaspar, Surface texture detection with a new sub-mm resolution flexible tactile capacitive sensor array for multimodal artificial finger. *J. Microelectromech. Syst.* **29**, 629–636 (2020).
38. H.-K. Lee, S.-I. Chang, E. Yoon, A flexible polymer tactile sensor: Fabrication and modular expandability for large area deployment. *J. Microelectromech. Syst.* **15**, 1681–1686 (2006).
39. F. Bergner, P. Mittendorfer, E. Dean-Leon, G. Cheng, Event-based signaling for reducing required data rates and processing power in a large-scale artificial robotic skin, in *Proceedings of the 2015 IEEE/RSJ International Conference on Intelligent Robots and Systems (IROS)* (IEEE, 2015), pp. 2124–2129.
40. C. Schürmann, M. Schöpfer, R. Haschke, H. Ritter, A high-speed tactile sensor for slip detection, *in Springer Tracts in Advanced Robotics* (Springer, 2012), vol. 76, pp. 403–415.
41. R. Kõiva, M. Zenker, C. Schürmann, R. Haschke, H. J. Ritter, A highly sensitive 3D-shaped tactile sensor, in *Proceedings of the 2013 IEEE/ASME International Conference on Advanced Intelligent Mechatronics* (IEEE, 2013), pp. 1084–1089.
42. C. Shao, S. Tanaka, T. Nakayama, Y. Hata, T. Bartley, Y. Nonomura, M. Muroyama, A tactile sensor network system using a multiple sensor platform with a dedicated CMOS-LSI for robot applications. *Sensors* **17**, 1974 (2017).

Funding: U.J. thanks the funding from the Basic Research Laboratory Program (NRF-2021R1A4A1021972) and S.-P.K. acknowledges the Brain Convergence Research Program (NRF-2019M3E5D2A01058328) through the National Research Foundation of Korea (NRF) funded by the MSIT. **Author contributions:** T.K., I.Y., S.-P.K., and U.J. conceived the concept and designed the experiments. T.K., I.Y., J.O., and U.J. designed the MIEC. T.K. and I.Y. analyzed the electrical property of the MIEC with equivalent circuit modeling. T.K. and J.O. characterized spike profile. T.K. designed the artificial sensory system. T.K. and J.K. measured PESS for dynamic stimuli. T.K., J.K., and S.-P.K. developed the simulator and real-time decoder. T.K., J.K., I.Y., S.-P.K., and U.J. cowrote the paper. **Competing interests:** There are patent applications in Korea (KR 10-2019-0053737), the United States (US17/434,100), and Japan (JP2021-557273) related to this work. The authors declare that they have no other competing interests. **Data and materials availability:** All data are available in the main text and/or the Supplementary Materials. The data and decoder code for this study have been uploaded to the following link: https://doi.org/10.5281/zenodo.5813317.

Submitted 22 July 2021
Accepted 19 January 2022
Published 16 February 2022
10.1126/scirobotics.abl5761

Science Robotics

Dynamic tactility by position-encoded spike spectrum

Taeyeong Kim, Jaehun Kim, Insang You, Joosung Oh, Sung-Phil Kim, and Unyong Jeong

Sci. Robot. **7** (63), eabl5761. DOI: 10.1126/scirobotics.abl5761

Science Robotics (ISSN 2470-9476) is published by the American Association for the Advancement of Science. 1200 New York Avenue NW, Washington, DC 20005. The title *Science Robotics* is a registered trademark of AAAS.